

1 **Technical note: „U-Th Analysis” – an open-source software** 2 **dedicated to MCICPMS U-series-data treatment and** 3 **evaluation**

4
5 Inga Kristina Kerber¹, Fabian Kontor¹, Aaron Mielke^{1,2}, Sophie Warken^{1,2}, Norbert Frank^{1*}

6 ¹ Institute for Environmental Physics, Heidelberg University, Heidelberg, Germany

7 ² Institute for Earth Sciences, Heidelberg University, Heidelberg, Germany

8 *Correspondence to:* Norbert Frank (<mailto:norbert.frank@iup.uni-heidelberg.de>)

9 **Abstract**

10 We present our standalone data analysis application for ²³⁰Th/U dating on multi-collector inductively coupled
11 plasma mass spectrometers (MC-ICP-MS). The Python-based algorithm is equipped with a graphical user
12 interface (GUI) and comprises raw data treatment, corrections, age calculation, and error estimation. Our
13 underlying measurement protocol employs a combination of Faraday cups (FC) and secondary electron multipliers
14 (SEM), and the software allows for different detector layouts for the measurement of the least abundant isotopes
15 ²³⁴U, ²³⁰Th and ²²⁹Th. We especially focus on features that ensure reproducibility and enable user-friendly
16 reanalysis of measurements such as customized calculation constants with templates. Result files are saved
17 automatically and contain all relevant settings used. Eventually, we demonstrate the relevance of adequate data
18 outlier treatment and generally recommend using the median instead of the mean of calculated ratios. The
19 performance of our evaluation software is demonstrated by a case study from a Puerto Rican stalagmite with
20 growth phases from modern to 40 ka old. The majority of the obtained ages reaches uncertainties in the range of
21 0.3-0.6%, underlining the capability of our measurement protocol.

22 **1 Introduction**

23 The U-series disequilibrium method, ²³⁰Th/U dating, is a precise chronometer covering approximately the last 650
24 kiloyears, and has proven indispensable for the age determination of marine and continental carbonate archives
25 and their applications (Bourdon et al., 2003). The method is based on a complete disequilibrium of ²³⁴U, with its
26 daughter nuclide ²³⁰Th, during the formation of secondary carbonates. It presumes a subsequent closed system
27 evolution of the activity ratio of (²³⁰Th/²³⁴U) and (²³⁴U/²³⁸U) since the time of formation. Ideally, the initial ²³⁰Th
28 activity of the material is presumed zero or can be estimated from the total Th concentration via an initial
29 (²³⁰Th/²³²Th) activity ratio. The dating applications for secondary carbonates and other appropriate materials are
30 manifold in geochemistry, archaeology, and climate science. Further development of this dating method includes
31 both improvements in instrumentation and measurement protocols, as well as reproducible data analysis and age
32 calculation schemes (Pourmand et al., 2014; Andersen et al., 2004; Cheng et al., 2013; Breton et al., 2015; Chiang
33 et al., 2019; Hellstrom, 2003; Hoffmann et al., 2007; Shen et al., 2002; Shen et al., 2012; Kerber et al., 2023; Shao
34 et al., 2019). The presently most sensitive and precise technology for high precision U and Th isotope
35 measurements is multi-collector inductively coupled plasma source mass spectrometry (MC-ICPMS). Recent
36 technological advances of MC-ICP-MS include the implementation of high ohmic amplifiers allowing to enhance

37 the dynamic range of multiple Faraday-collectors (FC) to six orders of magnitude for the simultaneous detection
38 of very large and low isotope abundances, instead of the conventionally used combination of secondary electron
39 multipliers (SEM) and FC (Breton et al., 2015). Measurement protocol updates aim at increasing measurement
40 precision and/or decreasing input sample masses by combining new detector layouts, improving the understanding
41 of correction factors, and ensuring a stable measurement environment (Cheng et al., 2013; Chiang et al., 2019;
42 Shen et al., 2002; Shen et al., 2012; Hellstrom, 2003; Andersen et al., 2004; Hoffmann et al., 2007; Kerber et al.,
43 2023; Shao et al., 2019).

44 We here focus on the third route for the enhancement of $^{230}\text{Th}/\text{U}$ dating, which is clear and reproducible data
45 analysis and age calculation schemes. Up to now, only two $^{230}\text{Th}/\text{U}$ dating data analysis routines have been
46 published (Shao et al., 2019; Pourmand et al., 2014). However, regarding the rising amount of data being produced
47 in MC-ICP-MS laboratories, data management is becoming more and more important. For example, some samples
48 might require later adaptation of the individual corrections of isotope ratios due to residual contamination with
49 non-carbonate material or detection of initial ^{230}Th from the carbonate forming environment.

50 Dating young materials of only a few years to centuries in age is challenging due to the small number of counts
51 on especially ^{230}Th , which implies that all correction factors including “ghost signal” corrections need to be
52 determined very precisely (Zhao et al., 2009; Chiang et al., 2019; Kerber et al., 2023). Regarding the removal of
53 scatter ions on the specific low abundance masses 230 and 229 amu, Kerber et al. (2023) demonstrated an effective
54 correction based on a linear dependence of the scattered ions on the ^{238}U signal. Other authors separate U and Th
55 chemically to reduce or remove the ^{238}U beam from the low abundance Thorium isotope measurements (Chiang
56 et al., 2019), which implies flexibility in the detector arrangement and data treatment protocol. As such scatter
57 peaks may depend on the specific instrument or vary through time, these corrections need to be adaptable constants
58 in the data evaluation routine. The influence on final atomic ratio and accuracy of the ghost signals as well as by
59 typical variation in other individual corrections such as peak tailing, mass fractionation, isobaric interferences are
60 evaluated in detail in Kerber et al. (2023).

61 In addition, the correction for initial Th may cause large age corrections and propagated uncertainties, in particular
62 since adequate initial Th values based on the $^{230}\text{Th}/^{232}\text{Th}$ ratio may be variable and difficult to detect (Hellstrom,
63 2006; Wenz et al., 2016; Wortham et al., 2022). There are different methods to estimate the initial Th isotope
64 ratio: First, isochrons can be used to determine the isotopic composition of the detrital component in the carbonate
65 (Ludwig and Titterton, 1994; Wenz et al., 2016; Stinnesbeck et al., 2020; Töchterle et al., 2022). Secondly,
66 analyses of modern drip waters or recent carbonate deposits allow estimation of the value and sources of initial
67 Th (Wortham et al., 2022; Li et al., 2022). In some cases the “true” age of a stalagmite can be also inferred from
68 other dating methods, such as radiocarbon (Akers et al., 2019; Huang et al., 2024) or the stratigraphic order
69 (Hellstrom, 2006). Also, several approaches can be combined (Warken et al., 2020; Akers et al., 2016; Roy-
70 Barman and Pons-Branchu, 2016).

71 Other aspects are updating half-lives (such as e. g. from Cheng et al. (2000b) to Cheng et al. (2013)), which makes
72 re-evaluation of previously measured data necessary. These tasks are error-prone, in particular when they require
73 copy-and-pasting data in e. g. spreadsheets. Also, a clear and unified documentation of the applied constants and
74 the way of saving data is desirable. Additionally, the statistical methods, for example for outlier correction, should
75 undergo clear documentation. Altogether, this helps to report Th/U ages in a standardized way (Dutton et al.,
76 2017).

77 In this study, we present our user-friendly GUI and the underlying algorithm for data treatment and age
78 calculation. The software is currently optimized for ThermoFisher Neptune MC-ICP-MS instruments, but the
79 open-source code in principle allows adaptations to other setups and instruments. Methods to treat outliers in
80 measurement data are particularly highlighted. As a case study, we present newly obtained ages from a stalagmite
81 from Larga Cave, Puerto Rico, which shows a modern growth phase, as well as continuous deposition during the
82 last Glacial into the deglaciation, thus demonstrating the performance of our method for both very young and
83 older sample materials. Our protocol enables a precise determination of speleothem growth rates, which allows a
84 comparison to a coevally deposited stalagmite from the same cave highlighting the influence of in-cave processes
85 on speleothem growth rates. In particular, this dataset showcases how initial ^{230}Th correction models can be easily
86 tested with our here presented software and GUI, and how those influence speleothem chronologies.

87 2 Methods

88 2.1 Standards and reference materials

89 We use our in-house triple spike solution (TriSpike) with a ^{233}U concentration of (0.038556 ± 0.0000009) ng/g, a
90 ^{236}U concentration of (3.86778 ± 0.00009) ng/g and a ^{229}Th concentration of (0.018055 ± 0.000008) ng/g (2
91 standard error of the mean) (Kerber et al., 2023). For standard bracketing, we employ the Harwell-Uraninite 1
92 (HU-1) as a reference material. Its activity ratios ($^{230}\text{Th}/^{238}\text{U}$) and ($^{234}\text{U}/^{238}\text{U}$) are presumed to be 1, as it is a secular
93 equilibrium material. Abundance sensitivity and hydride correction are determined by measuring CRM-112A U
94 reference solution and an in-house ^{232}Th standard. The CRM-112A gravimetric standard solution has a ^{238}U
95 concentration of (4.3021 ± 0.0015) $\mu\text{g/g}$, while the inhouse ^{232}Th standard calibrated with TriSpike has a ^{232}Th
96 concentration of (505.8 ± 1.02) ng/g (2 σ uncertainties). CRM-112A solution is also used to track the values of
97 the two ghost signal constants, k_{229} and k_{230} (Kerber et al., 2023). For k_{229} , it is measured without addition of
98 TriSpike, while in the case of k_{230} , the spiked CRM-112A solution is employed. For age determination, the ^{230}Th
99 and ^{234}U decay constants determined by Cheng et al. (2013) are used. Ages are reported with 2 σ statistical standard
100 mean error, but do not include half-life uncertainties.

101 2.2 Chemical preparation and instrumentation

102 The chemical preparation of carbonate samples includes sample dissolution in ultra clean nitric acid, spiking with
103 TriSpike and two steps of wet column chromatographic ion exchange separation of U and Th from matrix elements
104 using Eichrom UTEVA resin (Douville et al., 2010; Wefing et al., 2017; Matos et al., 2015). Chemical blanks are
105 commonly below 0.4 fg for ^{234}U and 0.04 fg for ^{230}Th and Ca matrix concentrations are required to be below 10
106 ppm. For the mass-spectrometric measurement, samples are dissolved in 1 % HNO_3 and 0.05 % HF. All samples
107 were measured on a MC-ICP-MS (ThermoFisher Neptune Plus) at the Institute for Environmental Physics,
108 Heidelberg University (Germany). The desolvating system CETAC Aridus II is used as inlet.

109 The mass spectrometer is equipped with Faraday cups (FC) and a central secondary electron multiplier (SEM).
110 The central detector can be selected between the SEM and a FC connected to a $10^{13}\Omega$ amplifier. ^{238}U is measured
111 on a $10^{10}\Omega$ amplified resistor. All other FC are connected to $10^{11}\Omega$ amplifiers. The cup setting to collect isotope
112 signals on masses 238 to 229 is shown in table 2 in Kerber et al. (2023). The first cycle collects all U isotopes for
113 2 seconds, with ^{234}U on the central detector (FC/SEM). The second and third cycle collect the Th isotopes for 2

114 seconds integrations time, with ^{230}Th and ^{229}Th on the central SEM. These cycles are repeated for an optimal
115 number for each measurement.

116 A measurement sequence starts with the determination of abundance sensitivity and tailing on two different
117 solutions for both uranium and thorium. Each sample and standard measurement is preceded by a procedural blank
118 measurement to ensure that the background signal has gone back to a clean state. CRM-112A measurements are
119 carried out to track ghost signal values at the beginning and end of a measurement sequence. Samples are
120 bracketed with HU-1 as a reference material. Samples, standard, and procedural blanks are measured with the
121 same configuration.

122 Mass fractionation (or mass bias) is corrected via the natural ratio of $^{235}\text{U}/^{238}\text{U}$ due to the lack of natural Th
123 isotopes. In our setup, the ratio of the artificial isotopes $^{233}\text{U}/^{236}\text{U}$ ratio in the spike is monitored for double
124 checking the mass bias correction. The calibration of FC gain and SEM yield is described in detail in Kerber et
125 al., (2023): While there is an internal electronic calibration function for the calibration of $10^{10}\ \Omega$ and $10^{11}\ \Omega$
126 amplifiers, the $10^{13}\ \Omega$ amplifier in our setup is calibrated manually. For this, the gain factor is determined regularly
127 by measuring ^{235}U alternately on the $10^{13}\ \Omega$ and $10^{11}\ \Omega$ amplified cup. In an analogous manner, the SEM yield is
128 routinely determined by measuring ^{235}U alternating on the SEM and on a $10^{11}\ \Omega$ FC at a signal intensity of ~ 5
129 mV. Since HU-1 standards are measured with the same detector configuration in standard bracketing mode, the
130 observation of the ($^{234}\text{U}/^{238}\text{U}$) values of HU-1 measurements allows monitoring and manual optimization of gain
131 and yield values for each measurement sequence in the data analysis scheme.

132 In its current version, the GUI is written for this type of measurement protocol. Many adaptations, such as fewer
133 procedural blank measurements, other isotope ratios for mass fractionation correction or similar require small
134 changes in the code, but are easily feasible for users sufficiently competent in Python. Numerous MC-ICP-MS
135 instruments, measurement protocols, and cup configuration settings can be used for such isotope measurements.

136 Here, we have developed our data treatment and GUI for a quasi-simultaneous measurement of U and Th isotopes
137 as detailed previously (Kerber et al., 2023). We do not need to specify the number of cycles or the exact scheme
138 of the sequence as the software will extract this information from the data. However, the cup configuration matters.
139 Our method implies that U and Th isotopes are present in the final solutions, which requires a U isotope scattering
140 correction. This is not necessarily needed when measuring U and Th isotope solutions independently.
141 Nevertheless, the here presented open-source software can easily be adopted to other cup configurations or raw
142 data outputs from different instruments.

143 2.3 Speleothem sample description

144 Stalagmite B1 was collected in 2019 in Larga cave, Puerto Rico ($18^{\circ}19'\text{N}$ $66^{\circ}48'\text{W}$, 350msl, supplementary Figure
145 S1A) from a passage in the deep part of the cave connected to the “Collapse room”. The host rock overburden at
146 the location of the sample is about 40-60m. It is in total 60 cm long, and has an average diameter of 15 cm
147 (supplementary Figure S1B). The drip site was still active, and was monitored with spot measurements over
148 several years, revealing varying drip intervals between 2 s and >120 s. A total amount of 37.7 ml water from the
149 drip site of stalagmite B1 was analysed for its U and Th activity ratios. Samples for $^{230}\text{Th}/\text{U}$ dating of the
150 speleothem with typical input masses of 100-150 mg have been cut using a diamond wire saw along the growth
151 axis. Chemical preparation, mass-spectrometric measurements, data treatment and evaluation of drip water and
152 the speleothem samples followed the methods described in Kerber et al. (2023) and in this study.

153 Larga Cave is located in the north central karst region of Puerto Rico (supplementary Figure S1A). Previous work
154 including extensive cave air and drip monitoring has demonstrated that the cave is a valuable location to study of
155 the influence of changing climate on past rainfall patterns in the Western tropical Atlantic (Vieten et al., 2018a;
156 Warken et al., 2022b; Vieten et al., 2018b). In particular, the main passage of Larga Cave is subject to a seasonally
157 varying ventilation, which results in pCO₂ values of 600 ppm close to atmospheric values during winter, and
158 higher values up to 1800 ppm in summer (Vieten et al., 2016). In contrast, in the deep part of the cave, where also
159 stalagmite B1 was collected, ventilation is strongly muted, and cave air pCO₂ values are higher with values up to
160 2300 – 3600 ppm (Vieten et al., 2016). As a result of this ventilation regime, growth rates are expected to vary
161 both seasonally, but also between different locations inside the cave (Vieten and Hernandez, 2021). So far, two
162 speleothem records from Larga Cave are been published, where the most recent covers the past 500 years (Vieten
163 et al., 2024), and the second stalagmite grew during the period of 46.2-15.3 ka with a hiatus from 41.1 to 35.5 ka
164 (Warken et al., 2020). For ²³⁰Th/U dating of Larga speleothems, high initial Th contents have to be considered -
165 a phenomenon that regularly occurs in speleothem records from the Caribbean and Central American region
166 (Fensterer et al., 2010; Steidle et al., 2021; Moseley et al., 2015; Schorndorf et al., 2023; Stinnesbeck et al., 2020;
167 Beck et al., 2001; Akers et al., 2016; Rivera-Collazo et al., 2015).

168 3 Data treatment and analysis procedures

169 The whole analysis procedure from raw data treatment to age calculation is conducted in one GUI featuring three
170 tabs: ‘Input’ for isotopic ratio calculations, ‘Inspect’ for outlier correction of the signal and ‘Analysis’ for age
171 calculation. The source code is accessible at https://github.com/puahd/UTh_Analysis. It is based on the open
172 source PyQt5 Python library (<https://pypi.org/project/PyQt5/>). To execute the GUI, the user has to run the file
173 “main.py”. The folder https://github.com/puahd/UTh_Analysis/dist also contains a compiled .exe file for the GUI
174 (“UTh Data Analysis.exe”) as well as default configuration files (“constants – coral.cfg” and “constants –
175 stalag.cfg”). Input and output format of files are .csv or .xlsx. The GUI consists of three consecutive tabs, for which
176 the functionalities and the underlying calculations and processes will be described in the following.

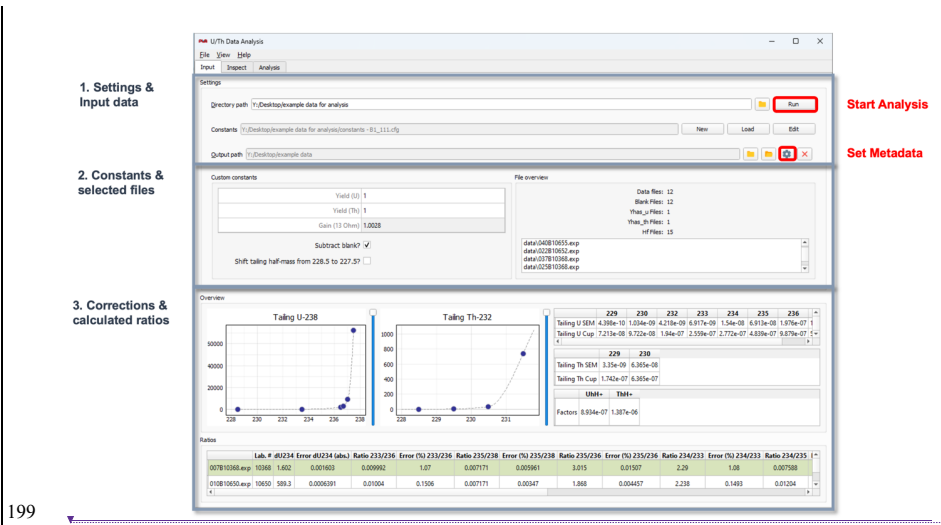
177 3.1 Input tab

178 In ‘Input’, as presented in [Figure 1](#), the user can navigate to the folder containing the raw mass spectrometer data
179 and start the calculation of corrected isotopic ratios (Box 1 in [Figure 1](#)). All tab screenshots present data from
180 stalagmite B1. Prior to the calculations, a configuration file containing all necessary constants used in the
181 calculations needs to be loaded (same Box 1). This file contains constants and correction factors used for
182 evaluation of the activity ratios and ages, such as mass fractionation coefficients, decay constants, the exact masses
183 of the isotopes and the values applied for initial ²³⁰Th correction model. All constants can be edited manually
184 either in the configuration file directly, or within the GUI using the button “edit”. An exemplary configuration
185 table is also provided in the supplementary material (Figure S2). To apply a ²³⁰Th correction model a value can
186 be set for the activity ratio and uncertainty of the contaminating material (“A230Th232Th Init.”). The
187 conventional approach to account for initial Th would be an activity ratio of 0.75 ± 0.38, assuming an upper
188 continental crust ²³²Th/²³⁸U weight ratio of 3.8 (Taylor and McLennan, 1985) with an uncertainty of 50% (Ludwig
189 and Paces, 2002) and ²³⁰Th, ²³⁴U, and ²³⁸U in secular equilibrium for the detrital material. Exemplary templates
190 for corals and speleothems with conventionally used correction models are provided. For speleothems, a typical

Deleted: Figure 1

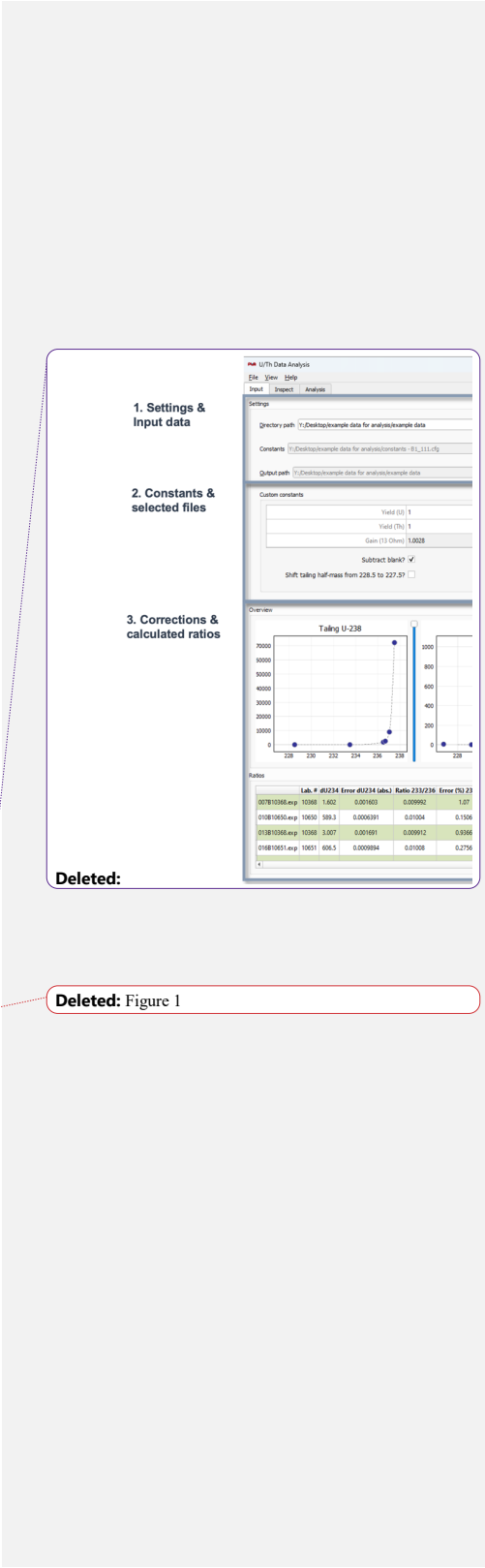
Deleted: Figure 1

193 activity ratio of ($^{230}\text{Th}/^{232}\text{Th}$)_{ini/detr} of detritus is estimated to 0.75 ± 0.38 (see above). Nevertheless, this ratio may
 194 require adjustment according to local conditions. The coral template assumes as default value an activity ratio of
 195 8 ± 4 , which is estimated for corals dwelling in waters of the northeast Atlantic upper thermocline (Wefing et al.,
 196 2017). For one data series, only one correction constant, the ($^{230}\text{Th}/^{232}\text{Th}$) activity ratio of the contamination, can
 197 be added to the calculation. Hence, in case several factors need to be explored, the data series requires repeated
 198 treatment.



199
 200 **Figure 1.** Input tab: (1) In the top part the data folder is selected (“directory path”), the constants file (“constants”) can be
 201 loaded (“load”), edited (“edit”), or created (“new”). In addition, it is possible to set an “output path”. Red boxes show the
 202 “settings” button to enter metadata for saving, as well as the “run” button to start the analysis. Box (2) shows the custom
 203 constants box as well as the file overview for the selected folder. In box (3), the plots on the top left show the interpolated
 204 tailing. On the top right, numerical values of U and Th tailing and hydride correction are presented. The calculated ratios are
 205 shown in the bottom panel.

206 **Figure 1,** shows the layout of the GUI ‘Input’ tab. Once the constants are implemented and the input data are
 207 selected, it is optional to choose an output path to store the analysis output (Box 1). If no path is specified, the
 208 results will be stored in the raw data folder. When clicking the settings button next to the output path (highlighted
 209 in red in Box 1), a menu opens in which the following parameters about the sample can be noted: denomination,
 210 type of archive, lab numbers, geographic origin, and a general description. The first and last laboratory number
 211 are automatically read out from the raw data. The final output result files will then be saved in a newly created
 212 folder under the name `_[labnumber1-labnumbern]` denomination in the directory chosen before. The metadata
 213 information transferred through the GUI dialogue window is stored in a .json file in the respective folder. In the
 214 ‘custom constants’ panel (Box 2), some settings can be selected, for example, if the blank has already been
 215 subtracted in the mass spectrometric software or not. Next to this panel, an overview over the files read in from
 216 the folder is shown. After running the evaluation script with the loaded data and adjusted settings (Button “run”,
 217 highlighted in red in Box 1), the results of tailing and hydride correction, respectively as well as the calculated
 218 ratios are displayed in the tab (Box 3). In addition, four excel .xlsx output files are created by the software at this
 219 stage and stored in the directory path folder: Ratios.xlsx, Tailing.xlsx, PrBlank.xlsx and Intensities.xlsx.



222 Ratios.xlsx contains all calculated ratios and their errors as also presented in the GUI (Box 3). Tailing.xlsx
223 summarizes the U and Th tailing values (in cps/V ^{238}U) for each mass. In PrBlank.xlsx, the average values for
224 each mass of the procedural blank measurements before each standard and sample are presented. Intensities.xlsx
225 contains the full data tables, with the signals in cps or V for each mass over all cycles. Every standard or sample
226 has its own sheet.

227 The algorithm of the 'Input' tab starts by reading in the '.exp' measurement files for sample and standard
228 measurements, process blank (=instrumental background) and Uranium and Thorium abundance sensitivity
229 measurements. The lines for all cycles for all isotopes are imported into a pandas data frame. Firstly, matrices for
230 tailing, hydride and process blank correction are produced that are later subtracted from the isotopic masses used
231 for ratio building. The individual steps are carried out as follows:

- 232 • Tailing: Uranium tailing is determined by measuring the off-masses 228.5, 233.5, 236.5, 236.7, 237.05
233 and 237.5 before a measurement sequence starts. The first half-mass can be changed between 228.5 and
234 227.5 as we observed a scatter peak around this mass that switched its exact position every few months.
235 Thorium tailing off-masses are 227.5, 228.5, 229.5, 230.5 and 231.5. For interpolation to full masses, we
236 use piecewise cubic Hermite interpolating polynomial fits (Kerber et al. 2023). The masses that undergo
237 ^{238}U tailing correction are ^{233}U , ^{234}U , ^{235}U , ^{236}U , ^{229}Th , ^{230}Th and ^{232}Th , while ^{232}Th correction is applied
238 to ^{229}Th and ^{230}Th .
- 239 • Hydride isobaric interference: Hydride correction is determined by measuring 239 amu for UH^+ and 233
240 amu for ThH^+ during the abundance sensitivity measurements. The instrumental background (or
241 memory) is here referred to as process blank. It is measured between all sample and standard
242 measurements for 70 s. Typical blank levels afterwards are 0.5 cps for ^{230}Th and 6 cps for ^{234}U . The
243 matrices from these three corrections are then used for data reduction of each isotope.
- 244 • Detector setting: Three main different detector layouts are possible and are detected automatically by the
245 software: 1) all isotopes on cup, 2) ^{234}U , ^{230}Th and ^{229}Th on SEM and 3) ^{234}U on FC, ^{230}Th and ^{229}Th on
246 SEM. In normal operation, option 2) and 3) are used, depending on the ^{234}U concentration of the
247 respective samples. ^{234}U signals above 2 mV are measured on the center FC which is the case for the
248 absolute majority of samples.

249 The sample and standard data are corrected for yield, gain and mass fractionation, are now used for the calculation
250 of all relevant isotopic ratios followed by subsequent outlier tests, as described in Section 3.2.

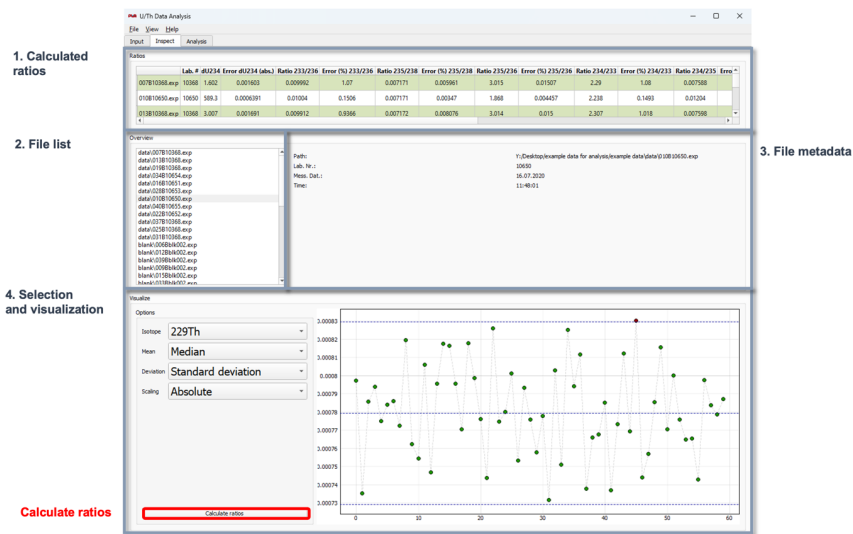
251 3.2 Inspect Tab

252 Following the initial raw data treatment in the Input Tab, the 'Inspect' tab (presented in [Figure 2](#)) allows to
253 visualize and retreat the data prior to final age calculation. In particular, the settings for the outlier test can be
254 adapted.

255 The Inspect tab allows the user to plot the signal datapoints over the measurement cycle number for all isotopes
256 in the individual measurement files of the sequence. In the top of the tab (1), the ratio results table from the 'Input'
257 tab is presented. On the left (2), the list of measurement files (.exp) is shown. By clicking on a specific file, the
258 metadata and the signal plotted over the measurement cycle number are presented (3). On the bottom left (4), four
259 dropdown menus are available: The first one, "Isotope", allows to select one isotope from all of the isotope species

Deleted: Figure 2

261 measured. “Mean” offers to switch between mean and median of the signal. The “Deviation” menu provides three
 262 options for the assessment of data dispersion: standard deviation, median absolute deviation and interquartile
 263 range. By setting “Scaling” to absolute or relative, the y-axis of the plot on the right can be changed between
 264 signal intensities in V or cps and relative values. Any selection in the dropdown menus leads to an automatic
 265 update of the plot on the right. Mean resp. median, as well as the dispersion ranges are presented as blue dashed
 266 lines. Data points outside of the dispersion range are marked in red as outliers.



267
 268 **Figure 2:** Inspect tab. (1) Ratio results table (from Input tab), (2) Overview of measurement files in folder, (3) metadata of a
 269 selected file and signal over measurement cycle number for one isotope (which can be selected in (4)), (4) option selection
 270 panel for the signal plotting.

271 The “Calculate ratios” button provides the option to recalculate the ratios using the updated mean and deviation
 272 selection for all isotopes. The default settings are median and standard deviation. However, these updated options
 273 are then used to exclude outliers from the ratio arrays, not the signal intensity arrays themselves. This means that
 274 not necessarily exactly the same data points are marked as outliers in the signal intensity plots and will be
 275 excluded, but the ones where signal ratios of two isotopes are outside of the accepted deviation range. The option
 276 selected in “Mean” will then also be used to calculate the average of the isotope ratios. The method of calculating
 277 the uncertainty of outlier-corrected isotopic ratios via the standard error, however, is fixed. In total, the software
 278 provides three different options for dispersion, including (i) the standard deviation (s), (ii) the interquartile range
 279 (IQR) (Tukey, 1977), and (iii) the median absolute deviation (MAD) (Leys et al., 2013; Huber, 2004; Rousseeuw
 280 and Croux, 1993). For the calculation of the MAD we assume normal distributed data. The treatment of means of
 281 ratios may have undesirable statistical properties for low or fast changing signals (Ogliore et al., 2011; Mclean et
 282 al., 2016), which could be taken into consideration when updating the software.

283 3.3 Analysis tab

284 In a last step, age calculation is carried out in the ‘Analysis’ tab presented in Figure 3. Here, additional input data
 285 is necessary from the sample weight tables (1). There are several ways to import these tables: Either by clicking
 286 “Load” and navigating to the respective folder, or by manually creating the table directly in the GUI (“Create”).
 287 An exemplary weight table is provided in the supplementary data (Figure 1). In the panel “Metadata history”, the
 288 previously loaded sample weight tables in the directory path folder are shown, and can be directly imported. “Start
 289 Analysis” starts the data analysis and calculates the ages. Outputs are both presented in the GUI as result table
 290 and stored in an Results.xlsx file. In case an output path was specified, Results.xlsx is created both in the output
 291 and in the directory path folder. If the output path is missing, the file is only saved in the directory path folder. If
 292 an output directory has been created for specific lab numbers, all following analysis of these same files will be
 293 written to the same output directory, but not overwrite earlier Results.xlsx. The Results.xlsx has five sheets: *Inputs*,
 294 *Calc*, *Results*, *Constants* and *Options*. *Inputs* presents sample weight and metadata as well as the calculated ratios.
 295 In *Calc*, all steps of the age calculation such as concentrations and activity ratios are shown. *Results* is a summary
 296 of the most important calculation steps and final age values and the same table as is presented in the GUI as the
 297 results table in figure 3. *Constants* contains the whole list of values from the (potentially edited) '.cfg' file. In
 298 *Options* the average and dispersion measure option are stored.

299 The equations for activity ratios to calculate ages are implemented according to Ivanovich and Harmon (1992),
 300 with:

$$301 \left(\frac{^{234}\text{U}}{^{238}\text{U}} \right) (t) = \left(\left(\frac{^{234}\text{U}}{^{238}\text{U}} \right)_{init} - 1 \right) \cdot e^{-\lambda_{234}t} + 1 \quad (4)$$

$$302 \left(\frac{^{230}\text{Th}}{^{238}\text{U}} \right) = 1 - e^{-\lambda_{230}t} + \frac{\delta^{234}\text{U}}{1000} \cdot \left(\frac{\lambda_{230}}{\lambda_{230} - \lambda_{234}} \right) \cdot \left(1 - e^{-(\lambda_{230} - \lambda_{234})t} \right) \quad (5)$$

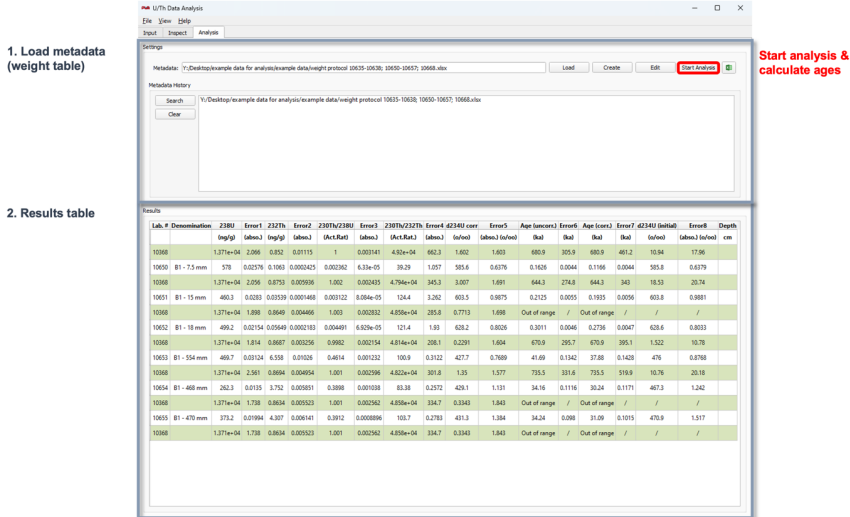
303 with

$$304 \delta^{234}\text{U} = \left(\left(\frac{^{234}\text{U}}{^{238}\text{U}} \right)_{meas} - 1 \right) \cdot 1000 (\text{‰}) \quad (6)$$

305 To obtain ages corrected for initial/detrital ^{230}Th , the $^{230}\text{Th}/^{238}\text{U}$ activity ratio used in eq. 5 is corrected using the
 306 initial $(^{230}\text{Th}/^{232}\text{Th})_{\text{ini/detr}}$ ratio and

$$307 \left(\frac{^{230}\text{Th}}{^{238}\text{U}}\right)_{\text{corr}} = \left(\frac{^{230}\text{Th}}{^{238}\text{U}}\right)_{\text{meas}} - \left(\frac{^{232}\text{Th}}{^{238}\text{U}}\right)_{\text{meas}} \cdot \left(\frac{^{230}\text{Th}}{^{232}\text{Th}}\right)_{\text{ini/detr}} \left(\frac{\lambda_{230}}{\lambda_{230}-\lambda_{234}}\right) \cdot e^{-\lambda_{230}t} \quad (7)$$

308 These equations need to be solved numerically. For the determination of age uncertainty, the usual approach is to
 309 repeat the numerical determination of the age for several thousand runs in a Monte-Carlo simulation while random
 310 sampling the input ratios from a normal distribution with μ corresponding to the ratio's value and σ corresponding
 311 to the uncertainty on this parameter.



312
 313 **Figure 3:** Analysis tab. (1) Load sample weight tables (metadata files). The bottom panel lists the history of previously loaded
 314 tables. The button highlighted in red starts the analysis to calculate ages ("Start Analysis") button. The panel in box (2)
 315 displays the results table.

316 **4 Example dataset: Stalagmite B1**

317 To demonstrate our data evaluation tool, we here present newly obtained ages of stalagmite B1 from Larga Cave,
318 Puerto Rico. The results of activity ratios and calculated ages can be accessed in the supplementary table S1.
319 Analysis of the speleothem samples reveals moderate U concentrations in the range between 300 and 600 ng/g,
320 and minor detrital ^{232}Th contamination with ($^{230}\text{Th}/^{232}\text{Th}$) activity ratios of typically >300 . However, in both the
321 top 20 mm and around 450 mm distance from top (dft) lower ($^{230}\text{Th}/^{232}\text{Th}$) activity ratios of c. 40 – 125 are
322 measured. U isotopic composition varies between 450 and 640 ‰ of $\delta^{234}\text{U}$ values. Uncertainties of the uncorrected
323 ages are typically in the range of 0.2 to 0.6 % (Table S1). Drip water shows high U concentration of 0.825 ng/g
324 and elevated initial Th concentrations, with an activity ratio of $K=(^{230}\text{Th}/^{232}\text{Th})=11.1 \pm 0.1$. We have used the
325 software to test how the chronology changes to assess the influence of a varying initial Th activity ratio. For this,
326 we used three different correction models, including the measured initial Th ratio of the drip water ($K=11.1 \pm$
327 0.1), the detrital correction value of $K=0.75 \pm 0.38$ derived from the bulk Earth crust chemical composition, as
328 well as a value of $K=23.7 \pm 7.5$ as previously determined using isochrons on speleothem PR-LA-1 from the same
329 cave (Warken et al. 2020). Figure S3 in the supplemental material shows the ages corrected for initial ^{230}Th using
330 the three different models. Only the initial ^{230}Th value measured in the drip water yields a stratigraphic order of
331 the corrected ages supporting the use of this value. Residual variability around the mean chronology increases and
332 age inversions appear in the record when using a different value of K. Figure S4 shows different growth models
333 for stalagmite PR-LA-B1. Growth rates vary between c. 10 and 150 $\mu\text{m/a}$, with highest values during the warm
334 Bolling–Allerød period c. 13.97 ± 0.051 and 13.114 ± 0.073 ka BP as well as the late Holocene growth phase after
335 0.277 ± 0.008 ka BP. Lowest growth rates occur during the final stage of Heinrich Stadial (HS) 1 (16.23 ± 0.082
336 to 13.97 ± 0.051 ka BP), HS3 (31.02 ± 0.10 to 29.38 ± 0.12 ka BP), and HS4 (40.81 ± 0.16 to 39.12 ± 0.12 ka
337 BP).

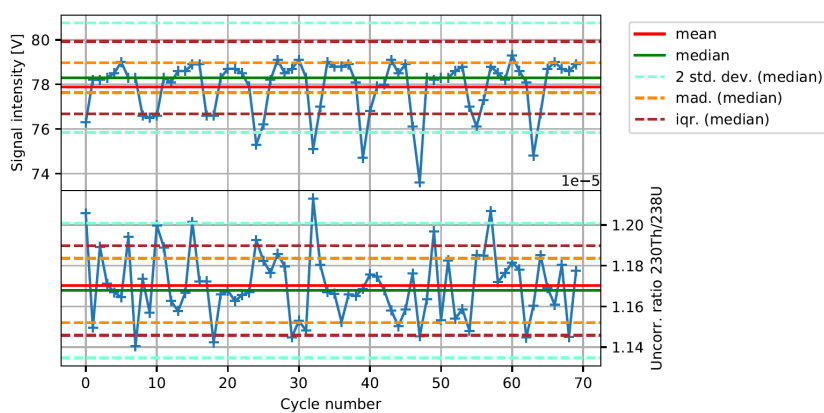
338 **5 Discussion**

339 **5.1 Outlier correction**

340 Outlier correction is carried out automatically by the software adapting the dispersion measure of the raw data
341 and in the following we argue that generally means should be replaced by medians. Shao et al. (2019) had
342 addressed this problem by implementing manual outlier removal by comparison to boxplots based on interquartile
343 ranges. We opted for the automatic version as this is more time efficient for large datasets. The different dispersion
344 measure options described in Section 3.2 are relevant because measurements are not always ideal cases with
345 normally distributed data and thus outliers. During measurements, short-term system instabilities occur for a
346 variety of reasons, such as varying gas flow in the inlet system, plasma instabilities, and varying size of sample
347 aerosols causing outliers in the signal intensities. Even though only the ratios between the different isotopes are
348 of interest, strong changes in signal intensity may lead to varying isotope ratios, as a result of changing variance.
349 Such difference may be amplified by the use of different detectors or with respect to different magnetic field
350 settings, which are not necessarily responding at exactly same amplitude. Moreover, signal decreases (detuning
351 events and temporal clocking) cause the statistical variance to increase locally.

352 **Figure 4**, shows an example: The upper panel displays periodic dips in the ^{238}U signal intensity during a
 353 measurement. In the lower panel of Fig. 4, the uncorrected ($^{230}\text{Th}/^{238}\text{U}$) activity ratio for the same measurement is
 354 plotted. For both curves, the different measures to calculate dispersion are shown. It is clearly visible that the
 355 median agrees much better with the majority of signal intensity values than the mean, which is strongly influenced
 356 by the periodic dips due to the asymmetry in the statistical distribution. Such an obvious difference is not visible
 357 in the isotope ratio, but within the resulting uncertainty. Consequently, we propose to generally use the median
 358 instead of mean by default. This is more accurate in the case of asymmetric small-scale oscillations inside the
 359 non-outlier interval and has no disadvantages.

Deleted: Figure 6



360
 361 **Figure 4:** Upper panel: ^{238}U signal intensities in Volt over measurement cycles for a carbonate sample during routine lab
 362 measurements. Lower panel: Corresponding uncorrected $^{230}\text{Th}/^{238}\text{U}$ ratio. Mean and median as well as the three different
 363 dispersion measures are plotted.

364 Applying standard deviation as a dispersion measure in **Figure 4** does not cover most of these outliers due to their
 365 large number and relatively small deviation. Thus, applying another dispersion measure for outlier removal is
 366 necessary here, and in addition more robust and easier to accomplish than manual deletion of all of the outliers. It
 367 is important, however, to stress that the outlier correction using the selected dispersion option is run on the
 368 calculated ratios after correction, not on the signal intensities themselves. This implies that when all isotopes are
 369 affected in the same way, they pass the outlier test. This is, however, unlikely at least for ratios of isotopes
 370 measured in different magnetic field settings. The dispersion measure of the outlier corrected ratio array is the
 371 same in every case, as described above.

Deleted: Figure 4

372 5.2 Detrital thorium correction

373 Thorium correction is often crucial for studying carbonates where the correction is significant, but the initial ^{230}Th
 374 value is unknown, potentially variable, or when studying “dirty” carbonates such as tufa and travertine (Mallick
 375 and Frank, 2002; Hellstrom, 2006; Wenz et al., 2016). Several studies have shown that this correction is
 376 particularly important for speleothem records from the Caribbean and Central American region, where values
 377 where found including 2 ± 1 (Schorndorf et al., 2023) or 14 ± 4 (Moseley et al., 2015). In Larga Cave, initial
 378 ($^{230}\text{Th}/^{232}\text{Th}$) ratios are presumably even higher where (Warken et al., 2020) obtained a value of 23.7 ± 7.5 using

381 isochrons on a stalagmite from the cave. Besides the terrestrial regime, this aspect is also relevant for marine
382 archive such as corals, where studies propose a large range of seawater ($^{230}\text{Th}/^{232}\text{Th}$) activity ratios. While Cheng
383 et al. (2000a) set the range to 80 ± 80 for deep-sea solitary corals, and Frank et al. (2004) calculated 10 ± 4 from
384 seawater in the Eastern North Atlantic deep sea, values between 0.4 – 3.1 were determined for tropical corals
385 (Shen et al., 2008). The range of both absolute values and uncertainties for these widely studied archives is hence
386 enormous, and the choice of the appropriate correction model becomes particularly important, when (i) samples
387 are very young and have generated only small amounts of ^{230}Th from U-decay, or (ii) when ultra-high precision
388 is at play since any possible correction of the data contribute to the final age uncertainty. In our case study, we
389 have run the correction of the ages of stalagmite B1 using three different correction models (Table S1). The
390 resulting differences are visualized in Figure S3, and demonstrate the significant impact not only on absolute
391 corrected ages, but also their uncertainties. For the young age at 7 mm dft (0.0466 ± 0.0045 ka BP), the difference
392 in the absolute corrected age when using another correction factor than the drip water value of $K = 11.1 \pm 0.1$ is c.
393 ± 50 years, which corresponds to a relative difference in the order of 100% (compare Table S1). Another example
394 is the sample at 554 mm dft (37.81 ± 0.14 ka BP for $K=11.1 \pm 0.1$), for which the other correction models also lead
395 to substantially different ages of 41.37 ± 0.19 ka BP ($K=0.75 \pm 0.38$) and 33.3 ± 2.7 ka BP ($K=23.7 \pm 7.5$), hence the
396 differences are still in the range of c. 10%. Notably, the low relative error of the initial ($^{230}\text{Th}/^{232}\text{Th}$) activity ratio
397 of the drip water results in equally low uncertainties of the corrected age in the range of 0.4%. In contrast, the
398 relative uncertainty of the age corrected with $K=23.7 \pm 7.5$ increases to 8%. Our GUI permits an easy adjustment
399 of the initial ($^{230}\text{Th}/^{232}\text{Th}$) activity ratio for Th correction, which allows a direct assessment of the resulting
400 corrected ages and uncertainties, and provides thus a convenient basis for further comparisons of the data. The
401 use of a standardized software instead of handmade tuning reduces the susceptibility to potential errors, e.g., from
402 copy-pasting, and ensures reproducibility in case a re-evaluation of the data is required to a later stage.

403 5.3 In-cave comparison of speleothem growth rates

404 The high number and precision of $^{230}\text{Th}/\text{U}$ ages of speleothem B1 allows investigation of growth rates changes.
405 Comparison with northern hemispheric climatic changes suggests, that speleothem B1 growth is sensitive to
406 prominent millennial-scale temperature variability, with higher growth rate during warmer phases and vice versa.
407 In particular, during the cooler and drier Heinrich stadials (Warken et al., 2022a), growth rates are reduced. In
408 addition, the results allow a comparison of the two coeval stalagmites from Larga Cave as shown in Figure S4.
409 Overall, GRs of PR-LA-B1 are about 5 times lower than observed for PR-LA-1, where average annual growth
410 rates are up to several mm/a. The difference in mean GR is also reflected in the shape of both speleothems, with
411 PR-LA-1 exhibiting a large and variable diameter between c. 15 and 35 cm (Warken et al., 2020), while B1 is
412 thinner with a diameter of 10-15 cm (supplementary Figure S1B). Differences in speleothem growth rates and the
413 shape of a stalagmite may result from temperature, carbonate saturation, drip rate, and carbon dioxide contrast
414 between cave air and saturation concentration of drip water (Merz et al., 2022; Skiba and Fohlmeister, 2023;
415 Kaufmann, 2003; Dreybrodt, 1999). Ca concentrations in Larga Cave show no significant differences between
416 drip sites (Vieten et al., 2018a, Vieten et al., 2018b, Warken et al., 2022). Therefore, the amplified GR and larger
417 diameter of PR-LA-1 could be the result of the considerably lower $p\text{CO}_2$ values in the main passage than
418 compared to the back part of the cave (Vieten et al., 2016; Vieten and Hernandez, 2021), which facilitates
419 enhanced oversaturation of the drip water with respect to calcite, and hence, stronger degassing of CO_2 and
420 speleothem growth (Merz et al., 2022). Hence, the two stalagmites reveal growth differences potentially related
421 to ventilation conditions.

422 6 Conclusion

423 We here provide an algorithm combined with a user-friendly GUI application for the treatment of $^{230}\text{Th}/\text{U}$ MC-
424 ICP-MS data obtained by ThermoFisher Neptune instruments, and subsequent age calculation and correction. The
425 two so far published programs explicitly aimed at $^{230}\text{Th}/\text{U}$ dating data reduction and age calculation are both
426 written for ThermoFisher Neptune instruments as well. Pourmand et al. (2014) described a Mathematica routine,
427 distributed as a Computable Document Format (.cdf) file, while Shao et al. (2019) had published a Matlab
428 algorithm with GUI. We here have chosen to use Python for our algorithm and GUI to keep it open-source. The
429 advanced user might want to change settings, which makes an opensource language and libraries a major
430 advantage. However, the stand-alone executable .exe format of the GUI allows user-friendly handling also for
431 non-programming experts. Our program supports multiple types of detector configurations: the FC-FC based
432 approach as well as FC-SEM combining protocols. It is however adapted for combined Th and U measurements
433 in three magnetic field lines (compare Kerber et al. (2023)), but other methods (such as separate solutions for Th
434 and U) can be implemented with small changes in the code. Furthermore, we offer the first order Taylor derivation
435 as a time-saving option for uncertainty calculation of final ages. Our application is especially designed to take
436 reproducible and clear data management into account by a collection of methods: This includes that automatic
437 creation of folders containing the results files and information on the sample metadata is possible and that .xlsx
438 output files automatically contain all constants used for calculation, as well as the settings for outlier correction.
439 Manually changing input constants, e. g. correction, of initial/detrital Th does not require to go to the code directly.
440 So, the whole analysis scheme does not require any copy-and-pasting from one excel table to the other, and the
441 constants used for calculation are easy to update.

442 Lastly, we demonstrated our protocols and data analysis scheme by accurately measuring and evaluating 30
443 speleothem ages from Larga Cave, Puerto Rico. Analyses of the growth rates and comparison with a coevally
444 growing stalagmite from the same cave highlights the importance of in-cave processes for speleothem deposition
445 rates.

446 **Author contributions**

447 IK - conceptualized the work, created and tested the implementation and operation of the code, co - supervised
448 FK, who developed the code for the GUI and tested rigorously all corrections. NF - conceptualized the project,
449 supervised IK, and FK and quality controlled the Th U isotope measurements of PR-LA-B1. SW - conceptualized
450 the project, provided guidance on sample selection, verified the code and conceptualized the application. SW
451 further evaluated the resulting age data on PR-LA-B1 and supervised a student project during which these and
452 other data had been collected.

453 **Code availability**

454 The source code of “UTh Analysis” is accessible at https://github.com/puahd/UTh_Analysis. It is based on the
455 open source PyQt5 Python library (<https://pypi.org/project/PyQt5/>). To execute the GUI, the user has to run the
456 file “main.py”. The folder https://github.com/puahd/UTh_Analysis/dist also contains a compiled .exe file for the
457 GUI (“UTh Data Analysis.exe”) as well as default configuration files (“constants – coral.cfg” and “constants –
458 stalag.cfg”). Example data for the analysis can be found in the supplementary material to this publication.

Deleted:

Deleted:

459 **Data availability**

460 Results of speleothem B1 ²³⁰Th/U dating are available in the online supplementary material.

461 **Sample availability**

462 Sample material is available on request to swarken@iup.uni-heidelberg.de

463 **Competing interests**

464 At least one of the (co-)authors is a member of the editorial board of Geochronology.

465 **Disclaimer**

466

467 **Acknowledgements**

468 The authors are very thankful to the enormous support of the whole team of the research group „Physics of
469 Environmental Archives” at Heidelberg University. Special thanks go to R. Eichstädter and A. Schröder-Ritzrau

472 for continuous engagement in the laboratory work and quality control. J. Arps is thanked for the development of
473 a previous version of „UTh-Analysis“. We are particularly grateful to R. Vieten for continuous support of
474 speleothem research in Larga Cave. R. Vieten, N. Schorndorf, S. Therre and J. Förstel are thanked for their help
475 in the field and with sample collection. We greatly acknowledge the work of N. Schorndorf, J. Schandl, and J.
476 Gafrieller on the chronology of speleothem B1. J. Bühler, C. Roesch, and K. Rehfeld are thanked for providing
477 access and support with the age-depth modelling code. N. Frank received financial support for ²³⁰Th/U
478 measurements (DFG Grant N°256561558) and for the installation of the MC-ICPMS facility (DFG Grant
479 N°247825108). S. Warken received financial support for the climate study of Puerto Rican speleothems via the
480 DFG (Grant N° 512385350) and by Heidelberg University via the Olympia Morata program.

481 **References**

482 Akers, P. D., Brook, G. A., Railsback, L. B., Liang, F. Y., Iannone, G., Webster, J. W., Reeder, P. P.,
483 Cheng, H., and Edwards, R. L.: An extended and higher-resolution record of climate and land use from
484 stalagmite MC01 from Macal Chasm, Belize, revealing connections between major dry events, overall
485 climate variability, and Maya sociopolitical changes, *Palaeogeography Palaeoclimatology*
486 *Palaeoecology*, 459, 268-288, 10.1016/j.palaeo.2016.07.007, 2016.

487 Akers, P. D., Brook, G. A., Railsback, L. B., Cherkinsky, A., Liang, F., Ebert, C. E., Hoggarth, J. A.,
488 Awe, J. J., Cheng, H., and Edwards, R. L.: Integrating U-Th, 14C, and 210Pb methods to produce a
489 chronologically reliable isotope record for the Belize River Valley Maya from a low-uranium
490 stalagmite, *The Holocene*, 29, 1234-1248, 10.1177/0959683619838047, 2019.

491 Andersen, M. B., Stirling, C. H., Potter, E. K., and Halliday, A. N.: Toward epsilon levels of
492 measurement precision on 234U/238U by using MC-ICPMS, *International Journal of Mass*
493 *Spectrometry*, 237, 107-118, 10.1016/j.ijms.2004.07.004, 2004.

494 Beck, J. W., Richards, D. A., Edwards, R. L., Silverman, B. W., Smart, P. L., Donahue, D. J., Herrera-
495 Osterheld, S., Burr, G. S., Calsoyas, L., Jull, A. J., and Biddulph, D.: Extremely large variations of
496 atmospheric 14C concentration during the last glacial period, *Science*, 292, 2453-2458,
497 10.1126/science.1056649, 2001.

498 Bourdon, B., Turner, S., Henderson, G. M., and Lundstrom, C. C.: Introduction to U-series
499 Geochemistry, *Reviews in Mineralogy and Geochemistry*, 52, 1-21, 10.2113/0520001 %J *Reviews in*
500 *Mineralogy and Geochemistry*, 2003.

501 Breton, T., Lloyd, N. S., Trinquier, A., Bouman, C., and Schwieters, J. B.: Improving Precision and
502 Signal/Noise Ratios for MC-ICP-MS, *Procedia Earth and Planetary Science*, 13, 240-243,
503 <https://doi.org/10.1016/j.proeps.2015.07.056>, 2015.

504 Cheng, H., Adkins, J., Edwards, R. L., and Boyle, E. A.: U-Th dating of deep-sea corals, *Geochimica*
505 *et Cosmochimica Acta*, 64, 2401-2416, [https://doi.org/10.1016/S0016-7037\(99\)00422-6](https://doi.org/10.1016/S0016-7037(99)00422-6), 2000a.

506 Cheng, H., Edwards, R. L., Hoff, J., Gallup, C. D., Richards, D. A., and Asmerom, Y.: The half-lives
507 of uranium-234 and thorium-230, *Chemical Geology*, 169, 17-33, 10.1016/s0009-2541(99)00157-6,
508 2000b.

509 Cheng, H., Lawrence Edwards, R., Shen, C.-C., Polyak, V. J., Asmerom, Y., Woodhead, J., Hellstrom,
510 J., Wang, Y., Kong, X., Spötl, C., Wang, X., and Calvin Alexander, E.: Improvements in ²³⁰Th dating,
511 ²³⁰Th and ²³⁴U half-life values, and U–Th isotopic measurements by multi-collector inductively
512 coupled plasma mass spectrometry, *Earth and Planetary Science Letters*, 371-372, 82-91,
513 10.1016/j.epsl.2013.04.006, 2013.

514 Chiang, H.-W., Lu, Y., Wang, X., Lin, K., and Liu, X.: Optimizing MC-ICP-MS with SEM protocols
515 for determination of U and Th isotope ratios and ²³⁰Th ages in carbonates, *Quaternary Geochronology*,
516 50, 75-90, 10.1016/j.quageo.2018.10.003, 2019.

517 Douville, E., Sallé, E., Frank, N., Eisele, M., Pons-Branchu, E., and Ayrault, S.: Rapid and accurate U–
518 Th dating of ancient carbonates using inductively coupled plasma-quadrupole mass spectrometry,
519 *Chemical Geology*, 272, 1-11, 10.1016/j.chemgeo.2010.01.007, 2010.

520 Dreybrodt, W.: Chemical kinetics, speleothem growth and climate, *Boreas*, 28, 347-356, 1999.

521 Dutton, A., Rubin, K., McLean, N., Bowring, J., Bard, E., Edwards, R. L., Henderson, G. M., Reid, M.
522 R., Richards, D. A., Sims, K. W. W., Walker, J. D., and Yokoyama, Y.: Data reporting standards for
523 publication of U-series data for geochronology and timescale assessment in the earth sciences,
524 *Quaternary Geochronology*, 39, 142-149, <https://doi.org/10.1016/j.quageo.2017.03.001>, 2017.

525 Fensterer, C., Scholz, D., Hoffmann, D., Mangini, A., and Pajón, J. M.: ²³⁰Th/U-dating of a late
526 Holocene low uranium speleothem from Cuba, *IOP Conference Series: Earth and Environmental*
527 *Science*, 9, 012015, 10.1088/1755-1315/9/1/012015, 2010.

528 Frank, N., Paterne, M., Ayliffe, L., van Weering, T., Henriot, J.-P., and Blamart, D.: Eastern North
529 Atlantic deep-sea corals: tracing upper intermediate water $\Delta^{14}\text{C}$ during the Holocene, *Earth and*
530 *Planetary Science Letters*, 219, 297-309, 10.1016/s0012-821x(03)00721-0, 2004.

531 Hellstrom, J.: Rapid and accurate U/Th dating using parallel ion-counting multi-collector ICP-MS,
532 *Journal of Analytical Atomic Spectrometry*, 18, 10.1039/b308781f, 2003.

533 Hellstrom, J.: U–Th dating of speleothems with high initial ^{230}Th using stratigraphical constraint,
534 *Quaternary Geochronology*, 1, 289-295, 2006.

535 Hoffmann, D. L., Prytulak, J., Richards, D. A., Elliott, T., Coath, C. D., Smart, P. L., and Scholz, D.:
536 Procedures for accurate U and Th isotope measurements by high precision MC-ICPMS, *International*
537 *Journal of Mass Spectrometry*, 264, 97-109, 10.1016/j.ijms.2007.03.020, 2007.

538 Huang, S., Cai, Y., Cheng, H., Xue, G., Cheng, X., He, M., Li, R., Ma, L., Wei, Y., Lu, Y., Yang, L.,
539 and Edwards, R. L.: An integrated study of constraining the initial ^{230}Th of a stalagmite and its
540 implications, *Quaternary Geochronology*, 80, 101497, <https://doi.org/10.1016/j.quageo.2024.101497>,
541 2024.

542 Huber, P. J.: *Robust statistics*, John Wiley & Sons 2004.

543 Ivanovich, M. and Harmon, R.: *Uranium series disequilibrium. Applications to environmental*
544 *problems*. Clarendon, 1992.

545 Kaufmann, G.: Stalagmite growth and palaeo-climate: the numerical perspective, *Earth and Planetary*
546 *Science Letters*, 214, 251-266, 10.1016/S0012-821X(03)00369-8, 2003.

547 Kerber, I. K., Arps, J., Eichstädter, R., Kontor, F., Dornick, C., Schröder-Ritzrau, A., Babu, A., Warken,
548 S., and Frank, N.: Simultaneous U and Th isotope measurements for U-series dating using MCICPMS,
549 *Nuclear Instruments and Methods in Physics Research Section B: Beam Interactions with Materials and*
550 *Atoms*, 539, 169-178, <https://doi.org/10.1016/j.nimb.2023.04.003>, 2023.

551 Leys, C., Ley, C., Klein, O., Bernard, P., and Licata, L.: Detecting outliers: Do not use standard
552 deviation around the mean, use absolute deviation around the median, *Journal of Experimental Social*
553 *Psychology*, 49, 764-766, <https://doi.org/10.1016/j.jesp.2013.03.013>, 2013.

554 Li, T.-Y., Wang, X., Chen, C.-J., Tan, M., and Wu, Y.: Testing the initial $^{230}\text{Th}/^{232}\text{Th}$ for “Known
555 Age Carbonate” and its significance for ^{230}Th dating and paleoclimate research, *Quaternary*
556 *International*, 607, 113-119, 2022.

557 Ludwig, K. and Paces, J.: Uranium-series dating of pedogenic silica and carbonate, Crater Flat, Nevada,
558 *Geochimica et Cosmochimica Acta*, 66, 487-506, 2002.

559 Ludwig, K. R. and Titterton, D. M.: Calculation of $(^{230}\text{Th}/\text{U})$ Isochrons, Ages, and Errors,
560 *Geochimica Et Cosmochimica Acta*, 58, 5031-5042, Doi 10.1016/0016-7037(94)90229-1, 1994.

561 Mallick, R. and Frank, N.: A new technique for precise uranium-series dating of travertine micro-
562 samples, *Geochimica et Cosmochimica Acta*, 66, 4261-4272, [https://doi.org/10.1016/S0016-](https://doi.org/10.1016/S0016-7037(02)00999-7)
563 [7037\(02\)00999-7](https://doi.org/10.1016/S0016-7037(02)00999-7), 2002.

564 Matos, L., Mienis, F., Wienberg, C., Frank, N., Kwiatkowski, C., Groeneveld, J., Thil, F., Abrantes, F.,
565 Cunha, M. R., and Hebbeln, D.: Interglacial occurrence of cold-water corals off Cape Lookout (NW
566 Atlantic): First evidence of the Gulf Stream influence, *Deep Sea Research Part I: Oceanographic*
567 *Research Papers*, 105, 158-170, 10.1016/j.dsr.2015.09.003, 2015.

568 McLean, N. M., Bowring, J. F., and Gehrels, G.: Algorithms and software for U-Pb geochronology by
569 LA-ICPMS, *Geochemistry, Geophysics, Geosystems*, 17, 2480-2496,
570 <https://doi.org/10.1002/2015GC006097>, 2016.

571 Merz, N., Hubig, A., Kleinen, T., Therre, S., Kaufmann, G., and Frank, N.: How the climate shapes
572 stalagmites—A comparative study of model and speleothem at the Sofular Cave, Northern Turkey,
573 *Frontiers in Earth Science*, 10, 10.3389/feart.2022.969211, 2022.

574 Moseley, G. E., Richards, D. A., Smart, P. L., Standish, C. D., Hoffmann, D. L., ten Hove, H., and
575 Vinn, O.: Early–middle Holocene relative sea-level oscillation events recorded in a submerged
576 speleothem from the Yucatán Peninsula, Mexico, *The Holocene*, 25, 1511-1521, 2015.

577 Ogliore, R., Huss, G., and Nagashima, K.: Ratio estimation in SIMS analysis, *Nuclear instruments and*
578 *methods in physics research section B: beam interactions with materials and atoms*, 269, 1910-1918,
579 2011.

580 Pourmand, A., Tissot, F. L. H., Arienzo, M., and Sharifi, A.: Introducing a Comprehensive Data
581 Reduction and Uncertainty Propagation Algorithm for U-Th Geochronometry with Extraction
582 Chromatography and Isotope Dilution MC-ICP-MS, *Geostandards and Geoanalytical Research*, n/a-
583 n/a, 10.1111/j.1751-908X.2013.00266.x, 2014.

584 Rivera-Collazo, I., Winter, A., Scholz, D., Mangini, A., Miller, T., Kushnir, Y., and Black, D.: Human
585 adaptation strategies to abrupt climate change in Puerto Rico ca. 3.5 ka, *The Holocene*, 25, 627-640,
586 10.1177/0959683614565951, 2015.

587 Rousseeuw, P. J. and Croux, C.: Alternatives to the Median Absolute Deviation, *Journal of the*
588 *American Statistical Association*, 88, 1273-1283, 10.1080/01621459.1993.10476408, 1993.

589 Roy-Barman, M. and Pons-Branchu, E.: Improved U–Th dating of carbonates with high initial ²³⁰Th
590 using stratigraphical and coevality constraints, *Quaternary Geochronology*, 32, 29-39,
591 <https://doi.org/10.1016/j.quageo.2015.12.002>, 2016.

592 Schorndorf, N., Frank, N., Ritter, S. M., Warken, S. F., Scholz, C., Keppler, F., Scholz, D., Weber, M.,
593 Aviles Olguin, J., and Stinnesbeck, W.: Mid-to late Holocene sea-level rise recorded in Hells Bells
594 $^{234}\text{U}/^{238}\text{U}$ ratio and geochemical composition, *Scientific Reports*, 13, 10011, 2023.

595 Shao, Q.-F., Li, C.-H., Huang, M.-J., Liao, Z.-B., Arps, J., Huang, C.-Y., Chou, Y.-C., and Kong, X.-
596 G.: Interactive programs of MC-ICPMS data processing for $^{230}\text{Th}/\text{U}$ geochronology, *Quaternary*
597 *Geochronology*, 51, 43-52, 10.1016/j.quageo.2019.01.004, 2019.

598 Shen, C.-C., Lawrence Edwards, R., Cheng, H., Dorale, J. A., Thomas, R. B., Bradley Moran, S.,
599 Weinstein, S. E., and Edmonds, H. N.: Uranium and thorium isotopic and concentration measurements
600 by magnetic sector inductively coupled plasma mass spectrometry, *Chemical Geology*, 185, 165-178,
601 [https://doi.org/10.1016/S0009-2541\(01\)00404-1](https://doi.org/10.1016/S0009-2541(01)00404-1), 2002.

602 Shen, C.-C., Wu, C.-C., Cheng, H., Lawrence Edwards, R., Hsieh, Y.-T., Gallet, S., Chang, C.-C., Li,
603 T.-Y., Lam, D. D., Kano, A., Hori, M., and Spötl, C.: High-precision and high-resolution carbonate
604 ^{230}Th dating by MC-ICP-MS with SEM protocols, *Geochimica et Cosmochimica Acta*, 99, 71-86,
605 10.1016/j.gca.2012.09.018, 2012.

606 Shen, C.-C., Li, K.-S., Sieh, K., Natawidjaja, D., Cheng, H., Wang, X., Edwards, R. L., Lam, D. D.,
607 Hsieh, Y.-T., Fan, T.-Y., Meltzner, A. J., Taylor, F. W., Quinn, T. M., Chiang, H.-W., and Kilbourne,
608 K. H.: Variation of initial $^{230}\text{Th}/^{232}\text{Th}$ and limits of high precision U–Th dating of shallow-water
609 corals, *Geochimica et Cosmochimica Acta*, 72, 4201-4223, 10.1016/j.gca.2008.06.011, 2008.

610 Skiba, V. and Fohlmeister, J.: Contemporaneously growing speleothems and their value to decipher in-
611 cave processes—A modelling approach, *Geochimica et Cosmochimica Acta*, 348, 381-396, 2023.

612 Steidle, S. D., Warken, S. F., Schorndorf, N., Förstel, J., Schröder-Ritzrau, A., Moseley, G. E., Spötl,
613 C., Aviles, J., Stinnesbeck, W., and Frank, N.: Reconstruction of Middle to Late Quaternary sea level
614 using submerged speleothems from the northeastern Yucatán Peninsula, *Journal of Quaternary Science*,
615 10.1002/jqs.3365, 2021.

616 Stinnesbeck, W., Rennie, S. R., Avilés Olguín, J., Stinnesbeck, S. R., Gonzalez, S., Frank, N., Warken,
617 S., Schorndorf, N., Kregel, T., and Velázquez Morlet, A.: New evidence for an early settlement of the
618 Yucatán Peninsula, Mexico: The Chan Hol 3 woman and her meaning for the Peopling of the Americas,
619 *Plos one*, 15, e0227984, 2020.

620 Taylor, S. R. and McLennan, S. M.: *The continental crust: its composition and evolution*, 1985.

621 Töchterle, P., Steidle, S. D., Edwards, R. L., Dublyansky, Y., Spötl, C., Li, X., Gunn, J., and Moseley,
622 G. E.: $^{230}\text{Th}/\text{U}$ isochron dating of cryogenic cave carbonates, *Geochronology*, 4, 617-627, 2022.

623 Tukey, J. W.: Exploratory data analysis, Reading, MA1977.

624 Vieten, R. and Hernandez, F.: StalGrowth—A Program to Estimate Speleothem Growth Rates and
625 Seasonal Growth Variations, *Geosciences*, 11, 187, 2021.

626 Vieten, R., Warken, S., Winter, A., Schröder-Ritzrau, A., Scholz, D., and Spötl, C.: Hurricane Impact
627 on Seepage Water in Larga Cave, Puerto Rico, *Journal of Geophysical Research: Biogeosciences*, 123,
628 879-888, 10.1002/2017jg004218, 2018a.

629 Vieten, R., Winter, A., Warken, S. F., Schröder-Ritzrau, A., Miller, T. E., and Scholz, D.: Seasonal
630 temperature variations controlling cave ventilation processes in Cueva Larga, Puerto Rico, *International*
631 *Journal of Speleology*, 45, 259-273, 10.5038/1827-806x.45.3.1983, 2016.

632 Vieten, R., Warken, S., Winter, A., Scholz, D., Miller, T., Spötl, C., and Schröder-Ritzrau, A.:
633 Monitoring of Cueva Larga, Puerto Rico—A First Step to Decode Speleothem Climate Records, in:
634 *Karst Groundwater Contamination and Public Health*, edited by: White, W. B., Herman, J. S., Herman,
635 E. K., and Rutigliano, M., *Advances in Karst Science*, Springer International Publishing, Cham, 319-
636 331, 10.1007/978-3-319-51070-5_36, 2018b.

637 Vieten, R., Warken, S. F., Zanchettin, D., Winter, A., Scholz, D., Black, D., Koltai, G., and Spötl, C.:
638 Northeastern Caribbean rainfall variability linked to solar and volcanic forcing, *Paleoceanography and*
639 *Paleoclimatology*, 39, e2023PA004720, 2024.

640 Warken, S. F., Vieten, R., Winter, A., Spötl, C., Miller, T. E., Jochum, K. P., Schröder-Ritzrau, A.,
641 Mangini, A., and Scholz, D.: Persistent Link Between Caribbean Precipitation and Atlantic Ocean
642 Circulation During the Last Glacial Revealed by a Speleothem Record From Puerto Rico,
643 *Paleoceanography and Paleoclimatology*, 35, 10.1029/2020pa003944, 2020.

644 Warken, S. F., Weißbach, T., Kluge, T., Vonhof, H., Scholz, D., Vieten, R., Schmidt, M., Winter, A.,
645 and Frank, N.: Last glacial millennial-scale hydro-climate and temperature changes in Puerto Rico
646 constrained by speleothem fluid inclusion $\delta^{18}\text{O}$ and $\delta^2\text{H}$ values, *Clim. Past*, 18, 167-181, 10.5194/cp-
647 18-167-2022, 2022a.

648 Warken, S. F., Kuchalski, L., Schröder-Ritzrau, A., Vieten, R., Schmidt, M., Höpker, S. N., Hartland,
649 A., Spötl, C., Scholz, D., and Frank, N.: The impact of seasonal and event-based infiltration on transition
650 metals (Cu, Ni, Co) in tropical cave drip water, *Rapid Communications in Mass Spectrometry*, 36,
651 e9278, <https://doi.org/10.1002/rcm.9278>, 2022b.

652 Wefing, A.-M., Arps, J., Blaser, P., Wienberg, C., Hebbeln, D., and Frank, N.: High precision U-series
653 dating of scleractinian cold-water corals using an automated chromatographic U and Th extraction,
654 *Chemical Geology*, 475, 140-148, 10.1016/j.chemgeo.2017.10.036, 2017.

655 Wenz, S., Scholz, D., Sürmelihindi, G., Passchier, C. W., Jochum, K. P., and Andreae, M. O.: $^{230}\text{Th}/\text{U}$ -
656 dating of carbonate deposits from ancient aqueducts, *Quaternary Geochronology*, 32, 40-52, 2016.

657 Wortham, B. E., Banner, J. L., James, E. W., Edwards, R. L., and Loewy, S.: Application of cave
658 monitoring to constrain the value and source of detrital $^{230}\text{Th}/^{232}\text{Th}$ in speleothem calcite:
659 Implications for U-series geochronology of speleothems, *Palaeogeography, Palaeoclimatology,*
660 *Palaeoecology*, 596, 110978, <https://doi.org/10.1016/j.palaeo.2022.110978>, 2022.

661 Zhao, J.-x., Yu, K.-f., and Feng, Y.-x.: High-precision ^{238}U – ^{234}U – ^{230}Th disequilibrium dating of the
662 recent past: a review, *Quaternary Geochronology*, 4, 423-433, 10.1016/j.quageo.2009.01.012, 2009.
663